Received: 6 May 2022 | Revised: 3 March 2023 | Accepted: 4 March 2023 | Published on: 2 April 2023

DOI: 10.1002/joc.8065

RESEARCH ARTICLE

International Journal of Climatology RMetS

Extreme temperatures detection and attribution related to external forcing in Madagascar

Luc Yannick Andréas Randriamarolaza[1,2] | **Enric Aguilar**[1] | **Oleg Skrynyk**[3]

[1]Center for Climate Change (C3), Institut Universitari de Recerca en Sostenibilitat, Canvi Climàtic i Transició Energètica (IU-RESCAT), Universitat Rovira i Virgili, Tarragona, Spain

[2]Direction Générale de la Météorologie, Antananarivo, Madagascar

[3]Ukrainian Hydrometeorological Institute, Kyiv, Ukraine

Correspondence
Luc Yannick Andréas Randriamarolaza, Center for Climate Change (C3), Institut Universitari de Recerca en Sostenibilitat, Canvi Climàtic i Transició Energètica (IU-RESCAT), Universitat Rovira i Virgili, Tarragona 43480, Spain.
Email: lucyannickandreas.randriamarolaza@estudiants.urv.cat and luc.randriamarolaza@gmail.com

Funding information
FORMAS (SE), DLR (DE), BMWFW (AT), IFD (DK), MINECO (ES), ANR (FR), European Union, Grant/Award Number: 690462

Abstract

In this article, we use standard extreme temperature indices to detect and attribute external forcing in Madagascar. These indices are calculated from observations and multi-model ensemble mean responses on anthropogenic-plus-natural (ALL), greenhouse gases (GHG), natural (NAT) and anthropogenic (ANT) which are subtracted from ALL and NAT forcings over 1950–2018. Correlation analysis emphasizes that the observed changes are more influenced by ENSO events, especially in minimum temperature. The observed changes are regressed or combined with model simulations from the sixth phase of the Coupled Model Intercomparison Project (CMIP6) to assess human impacts in indices. CMIP6 models with ALL, GHG and ANT forcings correspond well with the observations for the frequency indices than the intensity indices. Moreover, decadal trends indicate the existence of anthropogenic warming according to observations and multi-model ensembles with ALL, GHG and ANT forcings. Detection and attribution parties identify and justify the causes of the observed changes. We do this by performing the single-signal and two-signal analysis using the Regularized Optimal Fingerprinting (ROF) method with Total Least Square (TLS) regression. We estimate internal climate variability by means of control model simulations. As a result, we note an inconsistency in the warming trend with the NAT forcing. The influence of ALL, GHG and ANT forcings is detectable for standard extreme temperature indices between 1950 and 2018. Nearly, observed changes are attributed to GHG and ANT forcings except for coldest night and warm nights in Madagascar.

KEYWORDS
attribution, detection, extreme temperature indices, fingerprint, Madagascar, model simulations

1 | INTRODUCTION

During the last decades, the scientific community has identified global and regional warming trends. In this regard, IPCC AR6 indicates that global temperatures now are 1.07°C warmer than those from the preindustrial times. In Madagascar, the yearly mean of the minimum and maximum temperatures increased by 0.24°C/decade

and 0.21°C/decade, respectively (Randriamarolaza et al., 2021). Many authors have attempted to attribute the detected trends to human activities, for example, Santer et al. (1996) or Bindoff et al. (2013). However, most of the studies in D&A analysis focus on mid-latitudes. Otto et al. (2015), Peterson et al. (2012) or Peterson et al. (2013), stressed the lack of studies to attribute extreme climate events in Africa. Furthermore, the African continent suffers from poor quality and scarcity of observational data (Otto et al., 2013, 2015) which can interfere with the development adequate D&A studies. Nonetheless, Otto et al. (2020) provided some suggestions to address these problems. Following their advice, the purpose of this article is to apply the D&A analysis on extreme temperature changes in Madagascar by using a rare quality controlled and homogenized observational dataset (Randriamarolaza et al., 2021). Namely, we seek to understand the influence of external forcing (anthropogenic and natural) and to identify their robustness separately on extreme temperature changes. We apply a standard regression-based optimal fingerprinting approach, similar to Sonali and Kumar (2020). It is noteworthy that variant approaches exist depending on the transformation of the variables. For instance, a standard approach is applied directly with the indices by Morak et al. (2011, 2013), Christidis and Stott (2016) and Dong et al. (2018). Variables are converted to probability-based indices in Zhang et al. (2013), Min et al. (2013) and Kim et al. (2016) or fit an extreme value distribution in Wang et al. (2020) before implementing a standard approach. Since the majority of studies use the standard approach directly with the indices, we adopt it to simplify and facilitate the comparison of results. The remainder of this article is organized as follows: Section 2 describes the data and methodology. Section 3 presents key findings. Finally, Section 4 sets out both the discussion and the conclusion.

2 | DATA AND METHODOLOGY

2.1 | Observational data

For this study, we used the observational dataset of Malagasy daily minimum and maximum air temperatures developed by Randriamarolaza et al. (2021). The dataset contains 26 synoptic weather stations in Madagascar (see Table 1), quality-controlled with the INQC package (available at https://CRAN.R-project.org/package=INQC) and homogenized with the Climatol (available at https://CRAN.R-project.org/package=climatol) software. Inhomogeneities were detected at the monthly scale before adjusting daily data by interpolating monthly factors. Skrynyk et al. (2021) analysed the effects of Climatol homogenization on daily data and found substantial improvements in the accuracy and reliability of the temperature indices trends. Indices calculation was performed with ClimInd (Domínguez-Castro et al., 2020). The indices are categorized as intensity and frequency (see Table 2). Their anomalies were derived by subtracting a corresponding average value calculated based on the WMO reference period 1961–1990, as in Vincent et al. (2011) and Randriamarolaza et al. (2021). Subsequently, the regional anomaly time series were computed as the average of the anomalies across all stations. Lastly, regional anomaly series were smoothed using a 5-year moving average.

2.2 | Sea surface temperature data

The monthly Extended Reconstructed Sea Surface Temperature, version 5 (ERSST V5), with a resolution of 2° × 2° (Huang et al., 2017), was employed in our analysis in order to construct a time series of the El Niño Southern Oscillation Index (ENSO). Therefore, we delimited the ENSO region from 160° E to 80° W in longitude and from 5° S to 5° N in latitude. Sea surface temperature (SST) is averaged at all grid points of the ENSO region to obtain a single time series of monthly values. This time series is further used to compute the annual SST. The annual anomalies are then calculated according to the reference period 1961–1990. El Niño and La Niña events occur when SST anomalies are higher than 0.5°C and lower than −0.5°C, respectively (refer to Figure 1a). ENSO influence on the regional anomalies of the extreme temperature indices was analysed by using the Morlet wavelet function as in Torrence and Compo (1998) and Jevrejeva et al. (2003). Specifically, we used the wavelet coherence to measure the strength of the relationship between two time series as a function of frequency or period (see Section 2.4, for details). The performance of this method was highlighted by Torrence and Compo (1998), Yi and Shu (2012) and Liang et al. (2013). Figure 1b shows the wavelet power spectrum of the constructed ENSO index time series. ENSO events' cycle which is around 2–7 years can be clearly seen in the figure. The extreme ENSO events such as El Niño at 1982–1983 and 1997–1998 (also pointed out by Santoso et al., 2017) were captured by the wavelet transform.

2.3 | Model simulations data

Model simulation data sets on daily minimum and maximum temperatures, used to estimate the expected responses of the climate system to external forcings, were

TABLE 1 List of synoptic stations in Madagascar.

Stations	Longitude (°)	Latitude (°)	Elevation (m)	WMO numbers
Ambohitsilaozana	48.5	−17.7	786	67067
Analalava	47.8	−14.6	57	67019
Antalaha	50.3	−15.0	6	67025
Antananarivo	47.5	−18.9	1310	67085
Antsirabe	47.1	−19.9	1540	67107
Antsiranana	49.3	−12.4	105	67009
Antsohihy	48.0	−14.9	28	67020
Besalampy	44.5	−16.8	36	67037
Farafangana	47.8	−22.8	6	67157
Fianarantsoa	47.1	−21.5	1106	67137
Ivato	47.5	−18.8	1264	67083
Maevatanana	46.8	−17.0	77	67045
Mahajanga	46.4	−15.7	22	67027
Mahanoro	48.8	−19.8	5	67113
Maintirano	44.0	−18.1	25	67073
Mananjary	48.4	−21.2	6	67143
Morombe	43.4	−21.8	4	67131
Morondava	44.3	−20.3	8	67117
NosyBe	48.3	−13.3	11	67012
Ranohira	45.4	−22.6	823	67152
SainteMarie	49.8	−17.1	9	67072
Sambava	50.2	−14.3	5	67023
Taolagnaro	47.0	−25.0	8	67197
Toamasina	49.4	−18.1	6	67095
Toliary	43.7	−23.4	9	67161
Vohemar	50.0	−13.4	5	67017

TABLE 2 List of climate indices used in the study.

Category	Index	Indicator name	Definition	Unit
Intensity	TNn	Coldest night	annual minima of daily minimum temperature	°C
	TXn	Coldest day	annual minima of daily maximum temperature	°C
	TNx	Warmest night	annual maxima of daily minimum temperature	°C
	TXx	Warmest day	annual maxima of daily maximum temperature	°C
Frequency	TN10P	Cold nights	Percentage of days with Tmin <10th percentile	%
	TX10P	Warm nights	Percentage of days with Tmax <10th percentile	%
	TN90P	Cold days	Percentage of days with Tmin >90th percentile	%
	TX90P	Warm days	Percentage of days with Tmax >90th percentile	%
	TN1P	Very cold night	Count of days with Tmin <1st percentile	days
	TX99P	Very warm day	Count of days with Tmax >99th percentile	days

obtained from the Sixth Phase of the Coupled Model Inter-comparison Project (CMIP6) archive (available at https://esgf-node.llnl.gov/search/cmip6/, visited on December 9, 2020). CMIP6 historical model simulations differ depending on four elements: realization, initialization methods, perturbed physics and forcing. All

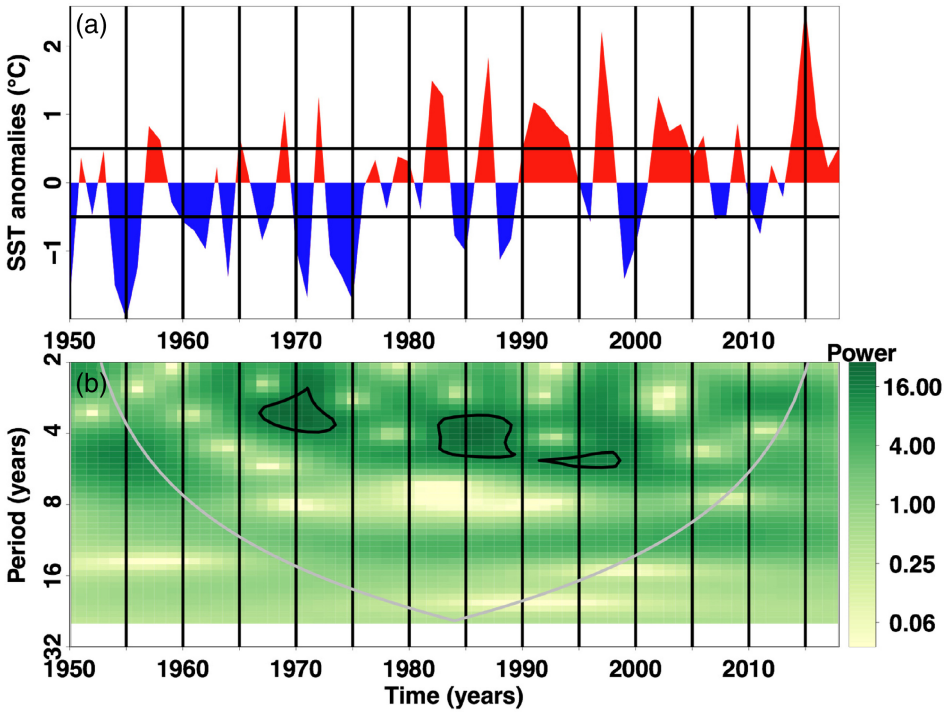

FIGURE 1 (a) Time series of ENSO index. (b) Wavelet power spectrum of ENSO index. The bold contours represent a significant area at level 0.05 against red noise. The cone of influence indicates where the effect of edge is important. [Colour figure can be viewed at wileyonlinelibrary.com]

TABLE 3 The number of model simulations per ensemble member.

	Minimum temperature				Maximum temperature			
Members	**ALL**	**GHG**	**NAT**	**CTL**	**ALL**	**GHG**	**NAT**	**CTL**
r1i1p1f1	4	8	8	12	5	4	4	11
r2i1p1f1	0	8	8	0	0	3	3	0
r3i1p1f1	3	8	8	0	3	4	4	0
r4i1p1f1	1	2	2	0	1	1	1	0
r5i1p1f1	1	2	2	0	1	1	1	0
r6i1p1f1	1	1	1	0	1	1	1	0
r7i1p1f1	1	1	1	0	1	1	1	0
r8i1p1f1	1	1	1	0	1	1	1	0
r9i1p1f1	1	1	1	0	1	1	1	0
r10i1p1f1	1	1	1	0	1	1	1	0
Total	14	33	33	12	15	18	18	11

historical model simulations with similar elements are grouped in an ensemble member. In our study, we choose 10 ensemble members with different realizations but similar initialization methods, perturbed physics and forcing.

Each ensemble member contained historical model simulations with anthropogenic-plus-natural (ALL), greenhouse gases (GHG) and natural (NAT) forcings. The GHG simulations represent climates with well-mixed greenhouse gases composed primarily of carbon dioxide, methane and nitrous oxide (Meinshausen et al., 2017). Table 3 shows that more than 50% of the runs were performed under the first three ensemble members. In addition, Table 4 illustrates that values of minimum and maximum temperatures were taken from 95 and 62 runs, respectively. These runs were produced using 19 models. However, only the ensemble member r1i1p1f1 had control or pre-industrial simulations (CTL runs). The most repeated model, which has more than 10% in all runs, is CanESM5 (Swart et al., 2019).

O'Neill et al. (2016) described the pathways of societal development, the Shared Socioeconomic Pathways (SSPs), as the future evolution of society with respective emissions scenarios used to drive climate models. Ssp245 is a central scenario in which trends continue their historical patterns without substantial deviations. The

TABLE 4 Numbers of model simulations for all ensemble members.

	Minimum temperature				Maximum temperature			
Models	**ALL**	**GHG**	**NAT**	**CTL**	**ALL**	**GHG**	**NAT**	**CTL**
ACCESS-CM2	0	0	0	1	0	0	0	1
ACCESS-ESM1-5	0	3	3	1	0	3	3	1
AWI-CM-1-1-MR	0	0	0	1	0	0	0	0
AWI-ESM-1-1-LR	0	0	0	1	0	0	0	1
BCC-CSM2-MR	0	3	3	0	1	2	2	0
CanESM5	8	10	10	0	8	10	10	0
CESM2	0	3	3	0	0	3	3	0
FIO-ESM-2-0	0	0	0	1	0	0	0	1
FGOALS-g3	2	3	3	0	3	0	0	0
HadGEM3-GC31-LL	0	0	0	1	0	0	0	1
MIROC6	1	3	3	0	1	0	0	0
MRI-ESM2-0	2	5	5	0	1	0	0	0
MPI-ESM-1-2-HAM	0	0	0	1	0	0	0	1
MPI-ESM1-2-HR	0	0	0	1	0	0	0	1
MPI-ESM1-2-LR	0	0	0	1	0	0	0	1
NESM3	1	0	0	0	1	0	0	0
NorES2-LM	0	3	3	1	0	0	0	1
NorESM2-MM	0	0	0	1	0	0	0	1
TaiESM1	0	0	0	1	0	0	0	1
Total	14	33	33	12	15	18	18	11

corresponding CMIP6 experiment ssp245 is considered as reference one in CMIP6-endorsed Model Intercomparison Projects (MIPs) and is employed to extend the historical simulation period beyond 2015 in detection and attribution MIP (O'Neill et al., 2016). For example, Gillett et al. (2016) used ssp245 to continue the historical simulation period to 2020. In our study, we selected model simulations that existed simultaneously in ssp245 and with ALL forcing for all members. As the historical simulation with ALL forcing period was only from 1850 to 2014 (Eyring et al., 2016), we extracted the time period over 1950–2014 then extended it from 2015 to 2018 by using ssp245. Thereafter, we uniformed their grid resolution to 1° by 1°.

A multi-model ensemble mean was built by averaging daily minimum and maximum temperature at each grid point of all model simulations and all members for each forcing, respectively. Therefore, regional time series were computed by averaging temperature over all grid points for multi-model ensemble mean with ALL, GHG and NAT. Thereafter, we computed annual indices by using ClimInd software for each grid point and regional time series. Annual index anomalies were calculated by taking WMO reference 1961–1990 as in the observational data. These steps were applied to all the considered runs (ALL, GHG, NAT and CTL). From these results, the anthropogenic (ANT) forcing was formed by subtracting ALL and NAT forcings. Therefore, ANT includes GHG and short-lived gases and aerosols. The CTL runs were split into two parts to create two independent estimations of internal variability, following Ribes et al. (2013). Finally, 5-year moving averages were calculated with regional average index anomaly time series for model simulations, CTL runs and multi-model ensemble means with ALL, GHG, ANT and NAT forcings.

2.4 | Methods

2.4.1 | Wavelet coherence

The wavelet analysis is often used to extract isolated and time-localized events (Lilly, 2017) or to analyse localized intermittent oscillation in time series. It also can be used to study the linkage between two time series (Grinsted et al., 2004). We use wavelet analysis, following the approach described in Torrence and Compo (1998), to assess the strength of relationship between observational intensity and frequency indices and ENSO index based on period or frequency. Torrence and Compo (1998)

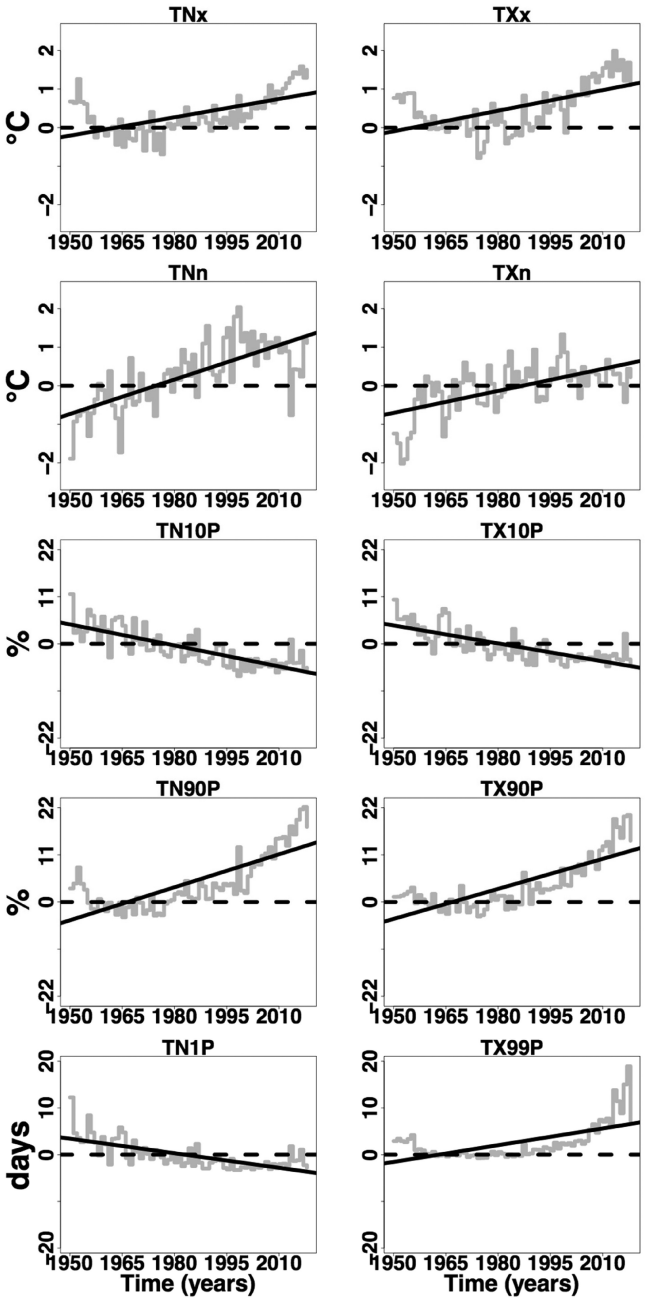

FIGURE 2 Regional average anomalies time series and the fitted trend lines for intensity and frequency indices over 1950–2018.

pointed out that the choice of a wavelet basis function was crucial, but it depended on the type of analysed data. The Morlet wavelet function is a complex sine-shaped Gaussian function, mostly employed with climate data, for example, by Yi and Shu (2012) and Ruwangika et al. (2020). We adopt it to derive the continuous wavelet transform of intensity and frequency indices' time series. Their significance correlation is assessed by using the wavelet coherence method. We use the R package 'biwavelet' (Tarik et al., 2018) to conduct this method.

2.4.2 | Trend calculation

We use trend analysis to quantify long-term changes over 1950–2018. As in Randriamarolaza et al. (2021), we use the Sen's slope method (Sen, 1968), implemented by Zhang et al. (2000) to calculate station-by-station and regional index trends and their confidence intervals. This approach is applied to observational time series, individual model simulations, CTL runs and multi-model ensemble mean with ALL, GHG, ANT and NAT forcings. The method is applied for each grid point to have spatial distribution of indices trends. The R package 'zyp', (Bronaugh & Werner, 2019), method, is used for calculation. This package has been employed in many articles such as Barry et al. (2018), Yosef et al. (2019, 2020) and Randriamarolaza et al. (2021). Besides, trends' sign comparison was done between multi-model ensemble mean and each model simulation. Then we filtered the grid points where 75% of model simulations under ALL, GHG, ANT and NAT forcings had the similar trends' sign and significant at 0.05 level than in multi-model ensemble mean under ALL forcing (see Figures 2 and 3).

2.4.3 | Standard optimal fingerprinting

The standard optimal fingerprinting method proposed by Allen and Tett (1999) and Allen and Stott (2003) with generalized linear regression Equation (1) is expressed as

$$Y = (X - \nu)\beta + \varepsilon, \quad (1)$$

where Y is observations, X is multi-model ensemble mean, ν is internal variability which is due to the interaction between atmosphere and ocean (Dima et al., 2005), β is scaling factor and ε is regression residual. It is used to quantify influences from external forcing. The amplitude of scaling factor measures presence or absence of signals in the observations. However, uncertainty arises mainly from quantification of internal climate variability of the climate system. Mostly, control simulations of climate models are used to assess the internal climate variability (Curry & Webster, 2011). Therefore, two independent noises from CTL runs are used to obtain the best estimate of scaling factors and their 5%–95% uncertainty levels (i.e., confidence intervals at 0.05 level) and to run the residual consistency check (RCC). RCC is performed to test the hypothesis if model simulation internal variability is consistent with observations. According to Stott et al. (2011), Dong et al. (2018) and Dileepkumar et al. (2018), if the best estimate of scaling factor and their uncertainty are greater than zero, we detect the influence of forcing. Besides, if the best estimate of scaling factor is

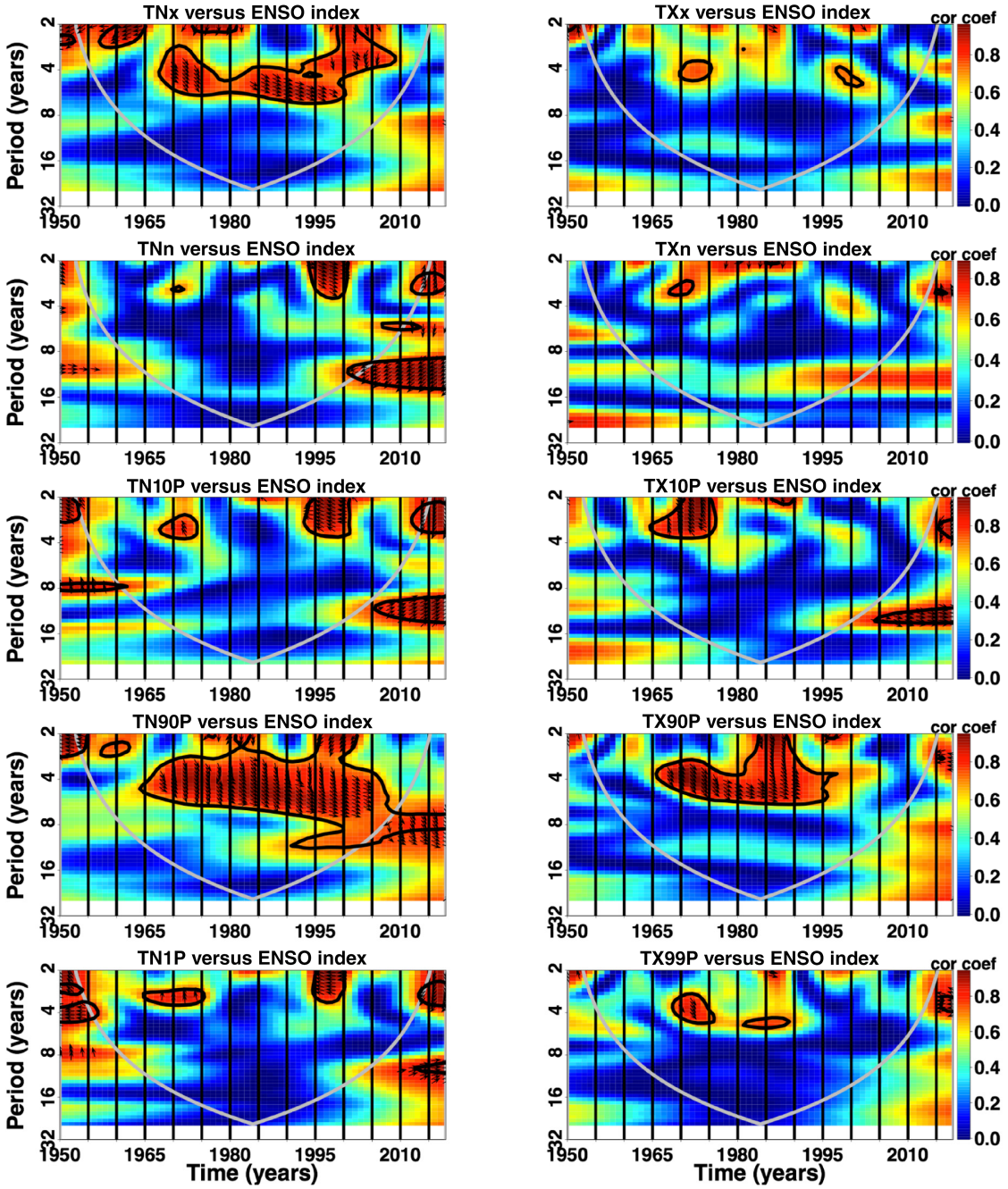

FIGURE 3 Wavelet coherence between intensity and frequency indices and ENSO events over 1950–2018. The bold contours represent a significant area at level 0.05 against red noises and right (left) arrows indicate if their direction is in phase (anti-phase). The cone of influence indicates where the effect of edge is important. Cor. coef. means correlation coefficient. [Colour figure can be viewed at wileyonlinelibrary.com]

consistent with the unit (i.e., scaling factor uncertainty interval contains the unit), we attribute an observed change to this forcing.

Ribes et al. (2013) developed an alternative to the standard optimal fingerprinting method called ' Regularized Optimal Fingerprinting (ROF)'. ROF method avoids the use of a truncated Empirical Orthogonal Function (EOF) projection to estimate the scaling factor β in the Equation (1). This method was used by Ribes et al. (2013), Wan et al. (2014), Lo et al. (2016) and Dileepkumar et al. (2018). It is implemented in the R Package ECOF-V1, which stands for Environment Canada's Optimal Fingerprint coded by Feng Yang (https://www.wcrp-climate.org/ictp-2014-tutorials. Accessed August 2, 2020), adapting the original code used in Ribes et al. (2013). We carry out single-signal and two-signal analyses by using

TABLE 5 Regional trends with its confidence intervals (in brackets) in the observations (OBS) and multi-model ensemble mean responses on anthropogenic-plus-natural (ALL), greenhouse gases (GHG) forcings over 1950–2018

		Decadal trends (confidence interval)		
Index	**Units**	**OBS**	**ALL**	**GHG**
TNn	°C/10 years	**0.29** (0.19,0.39)	**0.15** (0.12;0.19)	**0.17** (0.16;0.20)
TXn	°C/10 years	**0.11** (0.00;0.22)	**0.16** (0.13;0.19)	**0.17** (0.15;0.19)
TNx	°C/10 years	**0.24** (0.11;0.36)	**0.20** (0.16;0.25)	**0.20** (0.18;0.21)
TXx	°C/10 years	**0.23** (0.07;0.36)	**0.21** (0.17;0.26)	**0.22** (0.20;0.24)
TN10P	%/10 years	**−1.52** (−1.90;−1.18)	**−2.17** (−2.54;−1.80)	**−2.36** (−2.58;−2.17)
TX10P	%/10 years	**−1.31** (−1.72;−0.86)	**−2.24** (−2.62;−1.84)	**−2.28** (−2.51;−2.08)
TN90P	%/10 years	**3.01** (1.84;4.28)	**5.54** (1.20;2.65)	**4.42** (3.49;5.29)
TX90P	%/10 years	**2.38** (1.27;3.49)	**4.02** (2.78;5.25)	**3.72** (3.01;4.64)
TN1P	days/10 years	**−0.79** (−1.12;−0.49)	**−0.89** (−1.09;−0.72)	**−1.05** (−1.25;−0.85)
TX99P	days/10 years	**0.82** (0.17;1.54)	**1.09** (0.50;1.67)	**1.25** (0.73;1.97)

Note: Bold face indicates significant trends at 0.05 level.

the ROF method with Total Least Squares (TLS) regression as implemented in this package. On the one hand, the single-signal analysis performs the regression of the observations against the multi-model ensemble mean responses to ALL, GHG, ANT and NAT forcings, respectively. The objective is to check if the influence of each forcing can be detected in the observed changes. On the other hand, the two-signal analysis objective is to detect if the influence of ANT and NAT can be separated in presence of other signals. We use the 5-year moving averages of the regional anomaly time series of the observations and multi-model ensemble mean with ALL, GHG, ANT, NAT and CTL runs to carry out the D&A analysis over 1950–2018. This approach was used by Lu et al. (2018) to reduce data dimensionality.

3 | RESULTS

3.1 | Observed changes in extremes

Figure 2 shows regional indices anomalies and their trends. The changes in regional temperature extremes are significant at 0.05 level and in agreement with warming. Changes in intensity indices are similar except for TXn from 1950 to 2018. However, TNx and TXx increase at a faster rate than TNn and TXn. Warm-frequency events (i.e., indices related to maximum temperature) increase and cold-frequency events (i.e., indices related to minimum temperature) decrease. Similar as pointed out by Randriamarolaza et al. (2021), warm frequency events are changing with a faster rate than cold frequency events (see Figure 2). Observations' trend values ascertain these results (see Table 5). On the one hand, Figure 3 shows that intensity indices associated with minimum temperature are mostly correlated to ENSO events and they are in phase. This correlation may explain the peak of TNn around 1997/1998. On the other hand, frequency indices are mostly in phase with ENSO events except the TN90P, TN10P and TN1P (see Figure 3). On the other hand, intensity and frequency are well correlated to minimum and maximum temperatures at a 0.05 significance level, except for TXn (see Table 6). The cold nights (TN10P) and warm days (TX90P) have the highest correlation coefficients with minimum and maximum temperatures, respectively. Moreover, TN10P (TX90P) and minimum temperature (maximum temperature) evolve in the opposite direction (similar direction). However, the minimum and maximum temperatures only explain 76% and 82% of the variance of TN10P and TX90P, respectively.

3.2 | Spatial and temporal patterns in observations and simulations

Tables 5 and 7, presented in the previous section, shows also the regionally averaged trends for ALL, GHG, ANT and NAT forcings. On the one hand, trends of the multi-model ensemble mean under ALL, GHG and ANT forcings agree in sign and significance at 0.05 level with OBS, although OBS trends are mainly larger and smaller for intensity and frequency indices, respectively. We may explain this situation using Figure 4, which shows the Taylor diagrams (Taylor, 2001) and combines three parameters (standard deviation, root-mean-square [RMS]

TABLE 6 Correlation between temperature extremes and yearly mean of the minimum and maximum temperatures with 95% confidence interval.

	Yearly mean of minimum temperature		Yearly mean of maximum temperature	
Index	**Coefficient of correlation**	**Coefficient of determination**	**Coefficient of correlation**	**Coefficient of determination**
TNn	0.74 [0.61;0.83]	55%	0.64 [0.48;0.76]	41%
TXn	0.42 [0.20;0.60]	18%	0.48 [0.28;0.65]	23%
TNx	0.74 [0.61;0.83]	55%	0.74 [0.60;0.86]	54%
TXx	0.73 [0.60;0.82]	53%	0.78 [0.66;0.86]	60%
TN10P	−0.87 [−0.92;−0.80]	76%	−0.78 [−0.86;−0.66]	60%
TX10P	−0.77 [−0.85;−0.66]	60%	−0.81 [−0.88;−0.71]	66%
TN90P	0.86 [0.79;0.91]	75%	0.85 [0.77;0.90]	72%
TX90P	0.84 [0.75;0.90]	70%	0.90 [0.85;0.94]	82%
TN1P	−0.74 [−0.83;−0.61]	55%	−0.66 [−0.78;−0.50]	44%
TX99P	0.66 [0.51;0.78]	44%	0.72 [0.58;0.82]	52%

TABLE 7 Regional trends with its confidence intervals (in brackets) in the multi-model ensemble mean responses on anthropogenic (ANT) and natural (NAT) forcings over 1950–2018.

		Decadal trends (confidence interval)	
Index	**Units**	**ANT**	**NAT**
TNn	°C/10 years	**0.17** (0.14;0.19)	0.01 (−0.02;0.04)
TXn	°C/10 years	**0.17** (0.15;0.20)	0.01 (−0.03;0.05)
TNx	°C/10 years	**0.19** (0.16;0.21)	0.01 (−0;02;0.04)
TXx	°C/10 years	**0.21** (0.18;0.25)	0.00 (−0.03;0.04)
TN10P	%/10 years	**−2.22** (−2.58;−2.17)	0.01 (−0.21;0.88)
TX10P	%/10 years	**−2.27** (−2.50;−2.03)	0.02 (−0.25;0.30)
TN90P	%/10 years	**4.85** (3.85;5.84)	−0.11 (−0.53;0.63)
TX90P	%/10 years	**4.07** (3.25;4.91)	**−0.37** (−0.71;−0.05)
TN1P	days/10 years	**−0.99** (−1.16;−0.80)	0.06 (−0.08;0.20)
TX99P	days/10 years	**1.45** (0.94;2.05)	−0.15 (−0.31;0.00)

Note: Bold face indicates significant trends at 0.05 level.

difference and correlation coefficient) to match patterns between OBS and multi-model ensemble mean responses on ALL, GHG, ANT and NAT forcing. The amplitudes of variation (standard deviations) of OBS are greater and lower than multi-model ensemble means under ALL, GHG and ANT forcings for intensity and frequency indices, respectively. For instance, the coldest (warmest) day and night of the multi-model ensemble mean with ALL, GHG and ANT are less (well) correlated with OBS and have high (low) RMS. Their spatial interpolation of trends (Figures 5 and 6) indicates that more individual model simulations are in concordance with the multi-model ensemble mean for the warmest day and night compared to the coldest day and night. Besides, frequency indices of the multi-model ensemble mean with ALL, GHG and ANT forcings are well correlated with OBS. Nevertheless, warm events (TN90P, TX90P and TX99P) are more scattered than cold events (TN10P, TX10P and TN1P) of the multi-model ensemble mean with ALL, GHG and ANT forcings. In general, OBS changes are consistent with the multi-model ensemble mean responses on ALL, GHG and ANT forcings (see Figures 5 and 6). However, individual model and multi-model ensemble mean responses on ALL, GHG and ANT show discrepancies for some very extreme indices such as TN1P and TX99P. The North Western (NW) region is the hottest area in Madagascar and, in this region, the frequency of TXn and TX10P decrease and increase, respectively (see Figure 5). This situation is the opposite of the global warming effect. Therefore, it may be due to microclimate effects or to the homogeneity aspect and missing data filling in climate data records. On the other hand, the multi-model ensemble mean under NAT forcing trends are non-significant except for TX90P, with the

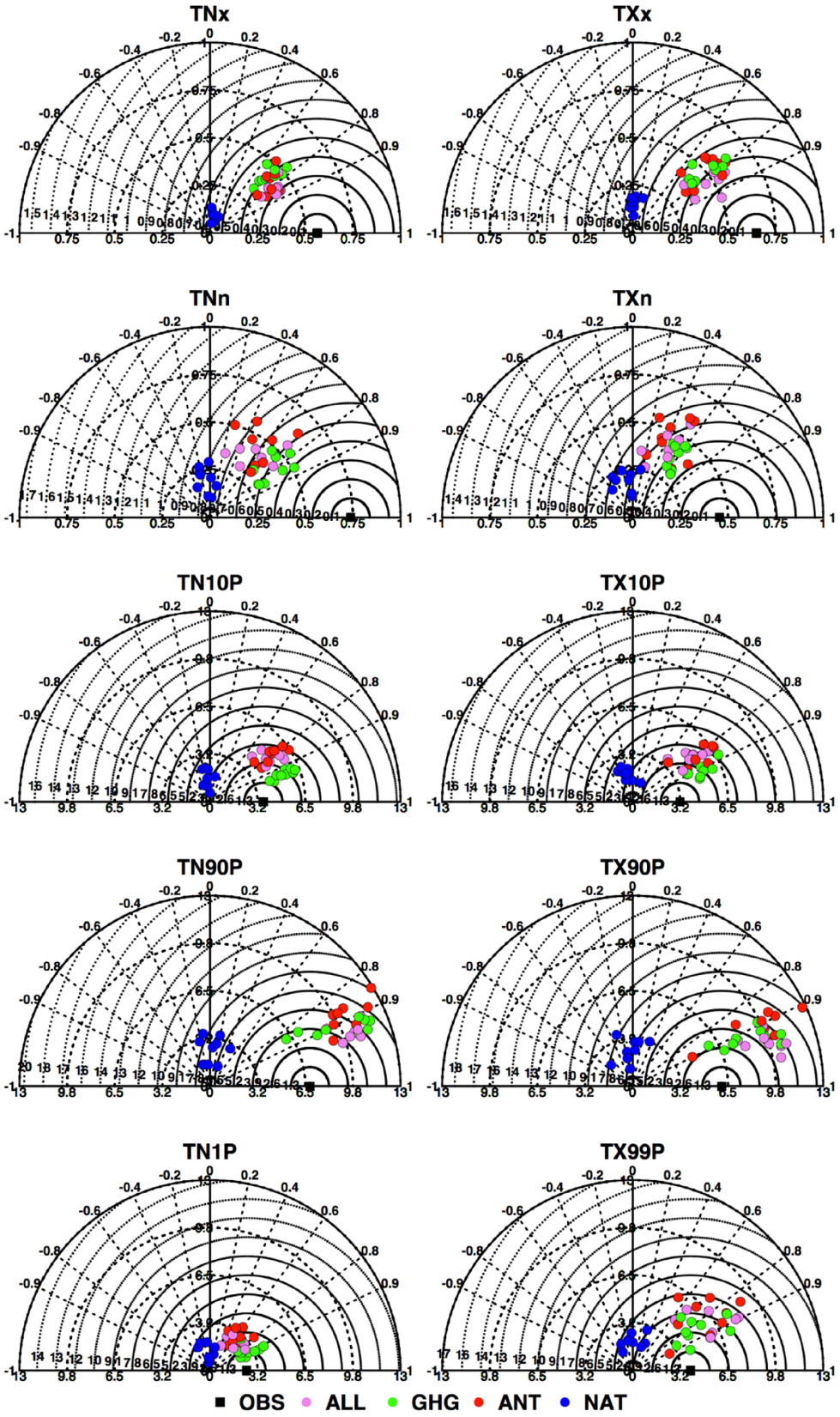

FIGURE 4 Taylor diagrams of intensity and frequency indices. The square on the x-axis indicates OBS considered as a reference. Dots indicate the 5-year mean regional of multi-model ensemble members under ALL, GHG, ANT and NAT forcings. Concentric circles from OBS and origin represent centred root-mean-square (RMS) difference and standard deviation, respectively. Radial axis indicates the correlation coefficients between OBS and ensemble member. [Colour figure can be viewed at wileyonlinelibrary.com]

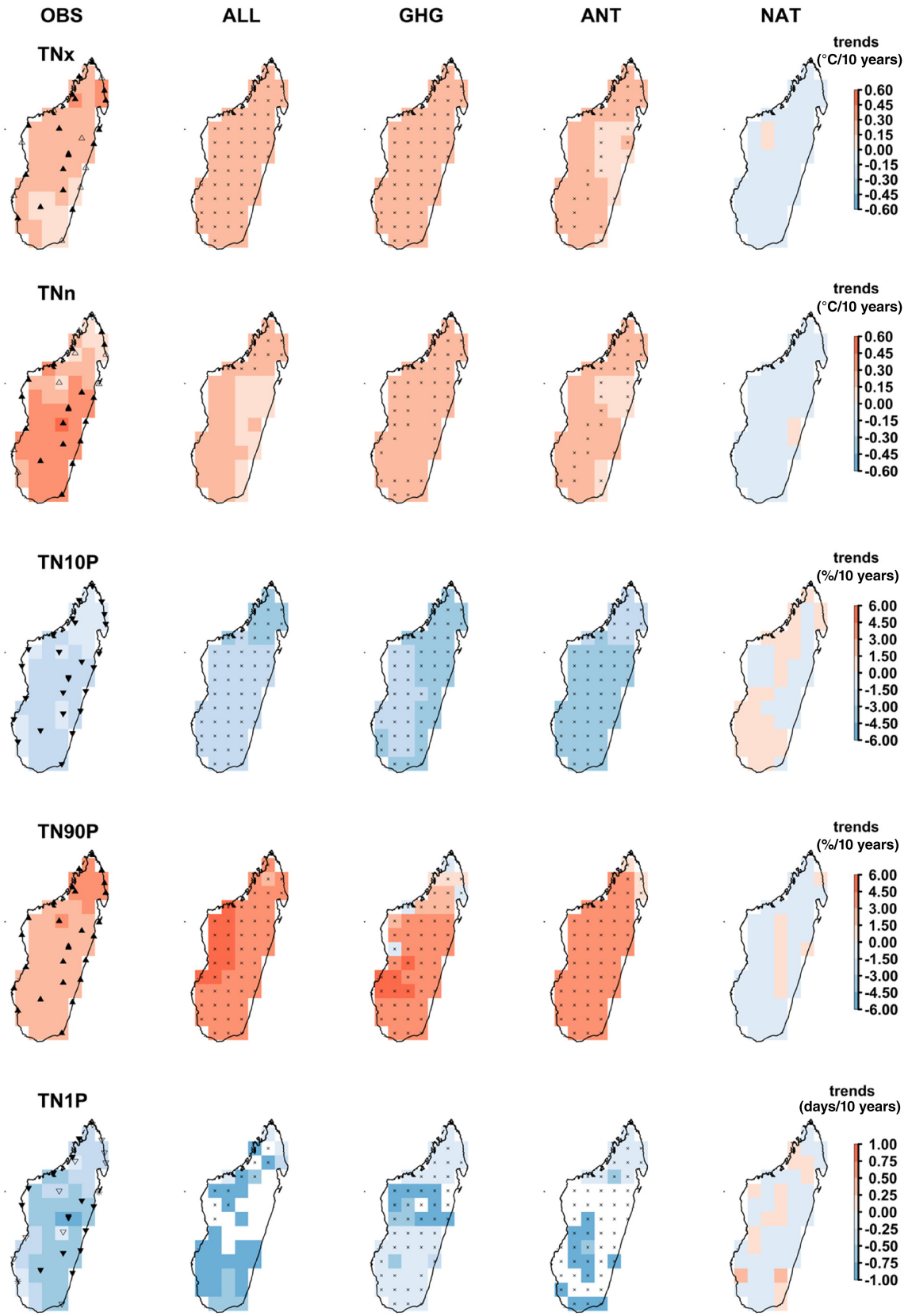

FIGURE 5 Spatial distribution trends over 1950–2018 of intensity and frequency indices related to minimum temperature in the observation and multi-model ensemble mean responses to ALL, GHG, ANT and NAT forcings. Crosses mark the agreement of at least 75% of the model simulations on the trends' significance at 0.05 level and sign with multi-model ensemble mean. [Colour figure can be viewed at wileyonlinelibrary.com]

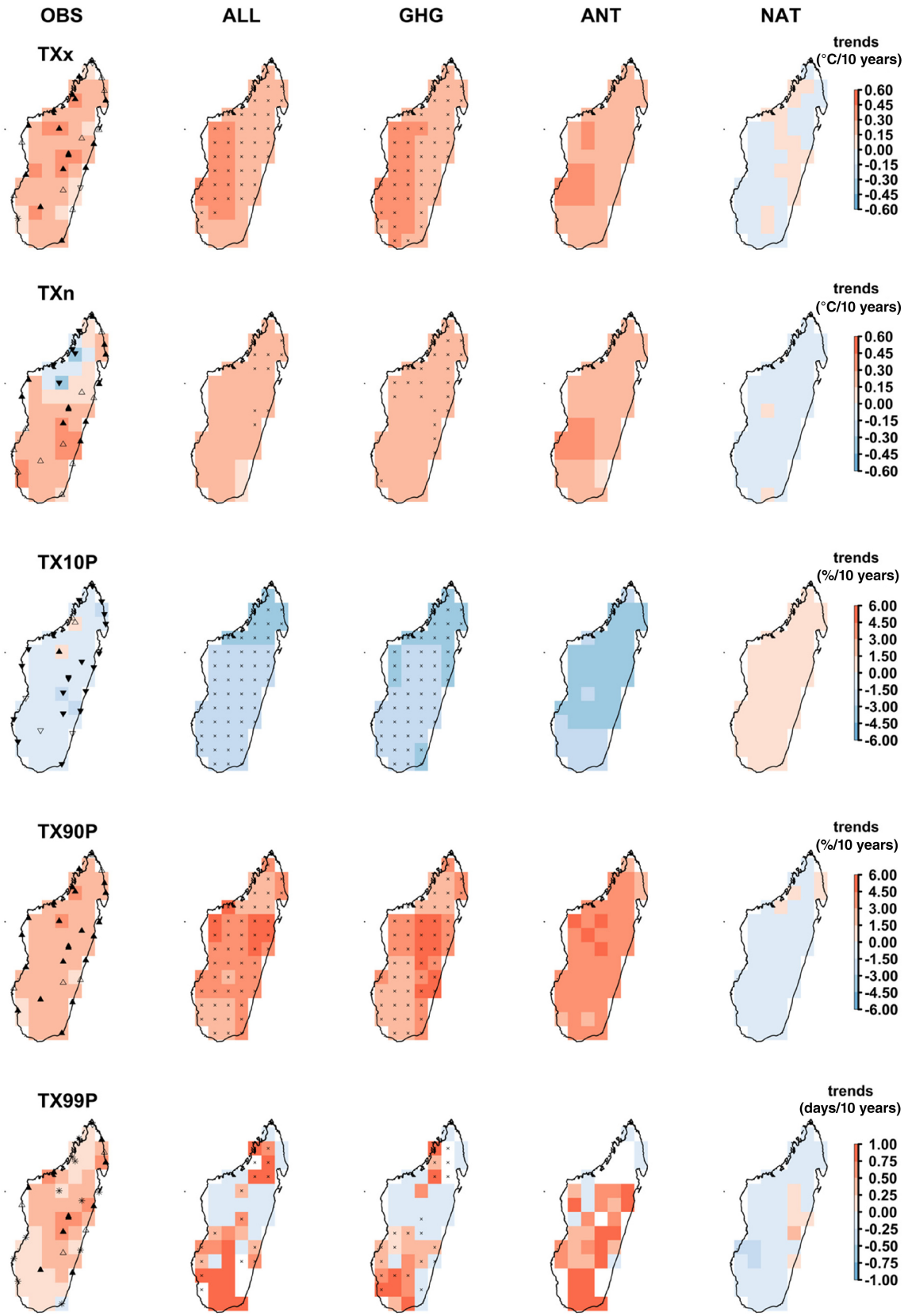

FIGURE 6 Spatial distribution trends over 1950–2018 of intensity and frequency indices related to maximum temperature in the observation and multi-model ensemble mean responses to ALL, GHG, ANT and NAT forcings. Crosses mark the agreement of at least 75% of the model simulations on the trends' significance at 0.05 level and sign with multi-model ensemble mean under ALL forcing. [Colour figure can be viewed at wileyonlinelibrary.com]

opposite sign to the other time series. Figure 4 shows any variation compared to OBS. Beyond this, any individual model under NAT forcing agrees with the multi-model ensemble mean under ALL forcing on indices trend sign and significance. Figure 6 shows a similar situation with ANT forcing related to intensity and frequency indices associated with maximum temperature. This is due to small numbers of individual models. Figure 7 represents the 5-year moving averages of the regional anomaly time series of the observational and multi-model ensemble means with ALL, GHG, ANT and NAT forcings over 1950–2018. Regional average anomaly time series of OBS are mainly included in the model simulation ranges (i.e., 5%–95%), especially for ALL, GHG and ANT forcings. On the contrary, the regional multi-model ensemble mean response on NAT forcing anomaly time series oscillate around the mean (see Figure 7).

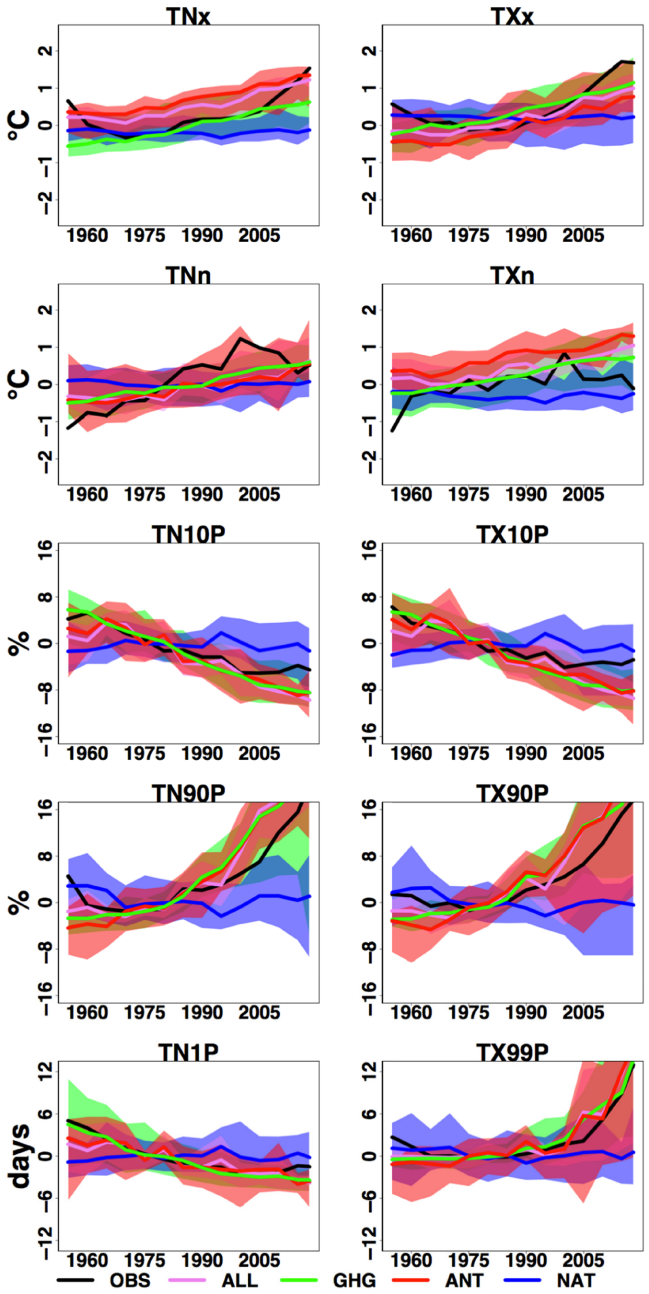

FIGURE 7 5-year moving averages of the regional anomaly time series of the observational and multi-model ensemble simulations. Shaded area show 5%–95% confidence interval of the selected model simulations. [Colour figure can be viewed at wileyonlinelibrary.com]

3.3 | Detection and attribution results

The single-signal analysis result is shown in Figure 8. It indicates that the intensity and frequency indices' scaling factors and lower limits of confidence intervals are greater than zero under ALL, GHG and ANT forcings. Therefore ALL, GHG and ANT influences are detected. Notice that observed changes are attributed to an external forcing if its influence is detected and the confidence interval of a corresponding scaling factor includes the unit. As ALL and ANT are composed by different forcing, single-signal analysis highlights this combined effect. On the one hand, observed changes of TXx, TNn, TN10P, TX10P, TN90P and TX90P are not attributed to ALL forcing. On the other hand, similar results are observed with ANT forcing except for TXx and TN10P. However, most observed changes are attributed to GHG forcing except for TNn and TX10P. Besides, observed changes of TNx, TXn, TN1P and TX99P are attributed to all external forcing except NAT. However, any external forcing is attributed to TNn and TX10P. Most RCC tests fail for NAT forcing except for TXx. It means that NAT forcing is inconsistent with observed changes.

We perform a two-signal analysis with ANT and NAT forcings to determine whether their influence can be detected separately. Figure 9 ascertains that NAT and ANT influences are detected for TXx and its observed changes are attributed only to ANT forcing. It also displays that observed changes of TNx, TN10P and TX99P are attributed to ANT forcing. On the contrary to single-signal analysis, observed changes of TX90P are attributed to ANT forcing. Moreover, observed changes of TNn, TXn and TN1P are inconsistent with ANT and NAT forcings. The other indices are consistent with NAT forcing even if NAT influence is not detected. In a nutshell, most observed changes are attributed to GHG and ANT forcings.

4 | DISCUSSION AND CONCLUSIONS

This article presents for a very first time a D&A analysis for Madagascar. Our results demonstrate that on the one

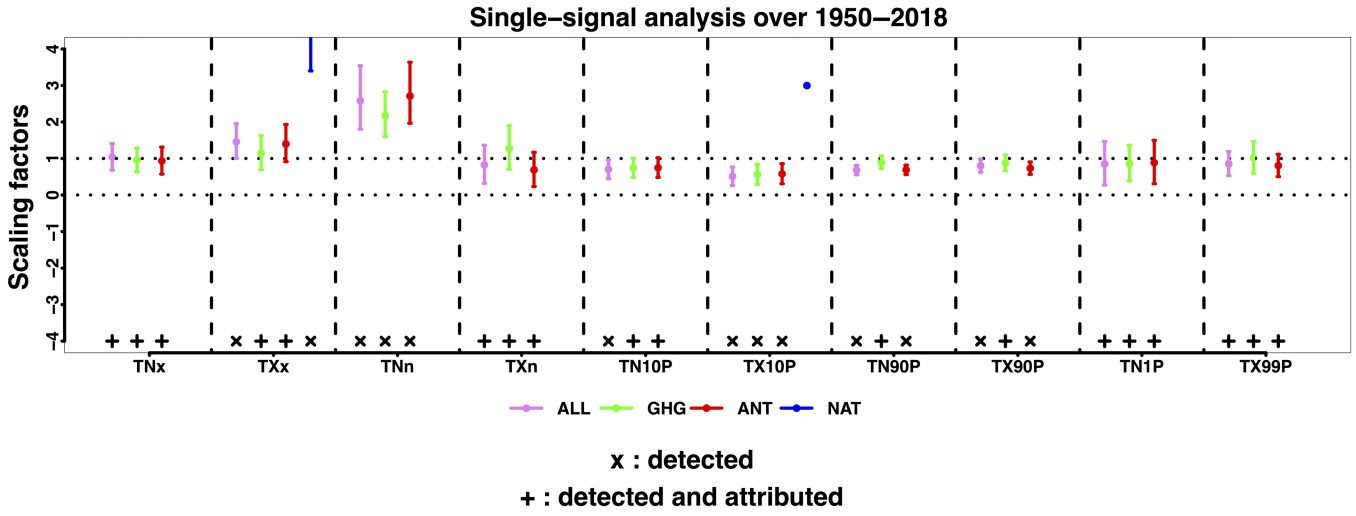

FIGURE 8 Single-signal analysis of best estimates of scaling factors (dots) and their 5%–95% uncertainty levels (bars) from multi-model ensembles under ALL, GHG, ANT and NAT forcings. If the residual consistency check (RCC) is failed or no detection found (scaling factor is less than zero), bars are missing. [Colour figure can be viewed at wileyonlinelibrary.com]

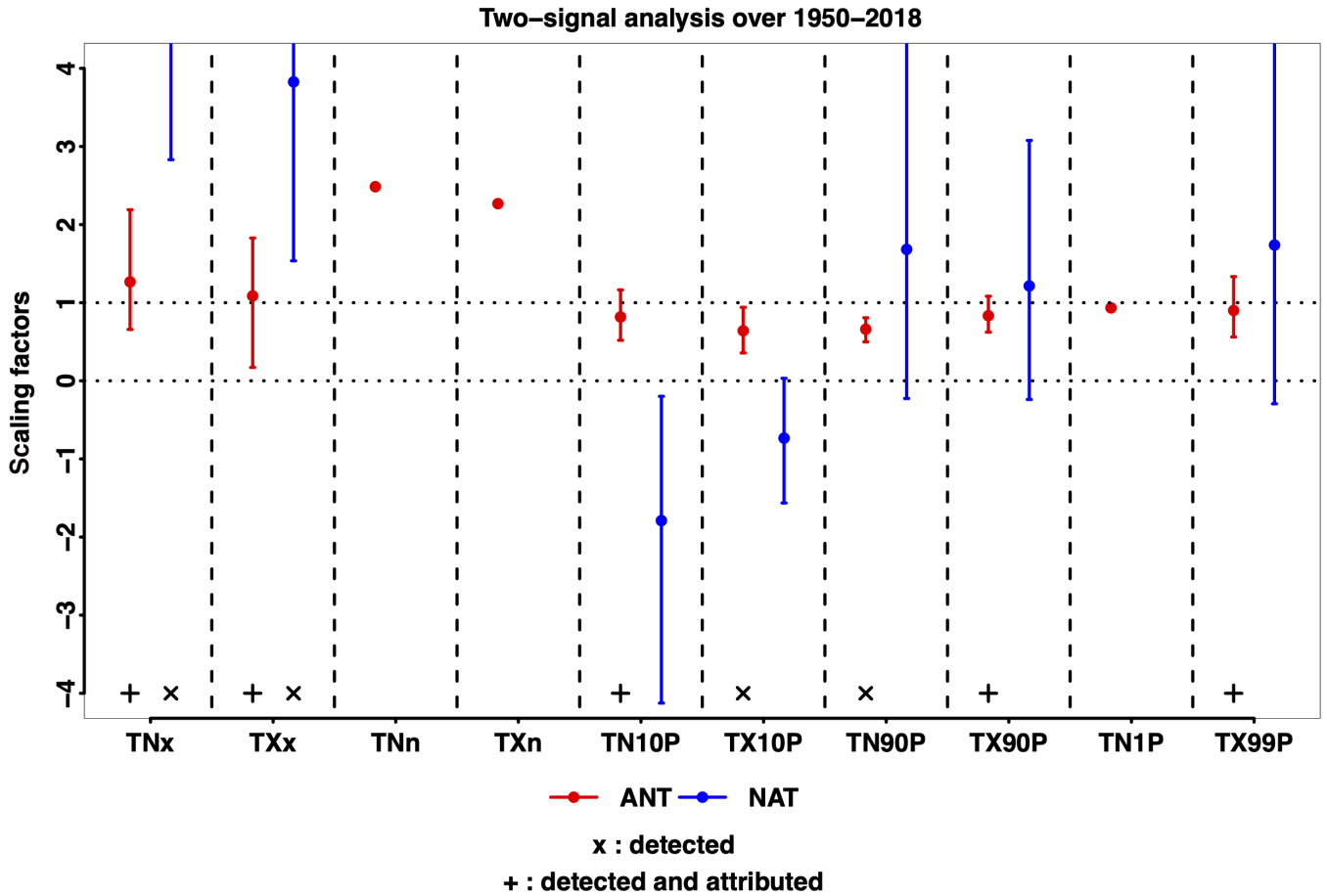

FIGURE 9 Two-signal analysis of best estimates of scaling factors (dots) and their 5%–95% uncertainty levels (bars) from multi-model ensembles under ANT and NAT forcing. If the residual consistency check (RCC) is failed or no detection found (scaling factor is less than zero), bars are missing. [Colour figure can be viewed at wileyonlinelibrary.com]

hand, regional and station-by-station trends in intensity and frequency indices point to the effects of global warming in Madagascar. Moreover, regional intensity and frequency indices are influenced by ENSO events, particularly indices associated with minimum temperature. On the other hand, observational and multi-model ensemble simulations with ALL, GHG and ANT forcings are well-matched in terms of regional intensity and frequency indices. Almost similar patterns are observed between OBS and multi-model ensemble members with ALL, GHG and ANT forcings, particularly for frequency indices, based on the Taylor diagram. However, any relationship found between OBS and multi-model ensemble members with NAT forcing. Spatial distribution of trends in intensity and frequency indices ascertain these findings. The ROF method demonstrates that the observed changes of intensity and frequency indices are mostly influenced by ALL, GHG and ANT forcings. Moreover, observed changes are mainly attributed to ANT and GHG forcings. Any observed changes in intensity and frequency indices are influenced by NAT forcing.

The state-of-the-art on D&A analysis recommends using a high-quality observational dataset (Coumou & Rahmstorf, 2012), so we used quality-controlled and homogenized observations of daily minimum and maximum temperatures (Randriamarolaza et al., 2021). According to Zhai et al. (2018), uncertainties might come from methods' selection in D&A analysis. In this article, we applied the standard optimal fingerprinting method by using ROF with TLS regression to drive single-signal and two-signal analyses against ALL, GHG, ANT and NAT forcings. ROF method used an inverse of the covariance matrix avoiding projection steps, providing improved accuracy (see Ribes et al., 2013). As underlined by Hannart et al. (2014), errors might arise from internal variability, model error or observational error in D&A analysis. They suggested that if all errors shared the same covariance, TLS was the best statistical method to perform D&A analysis. Nevertheless, the robustness of results was based on model simulations and statistical methods used as pointed out by Hegerl and Zwiers (2011) and Zhai et al. (2018). In this article, we selected model simulations, which contributed to the IPCC AR6 from the CMIP6 archive. Model simulations had similar initialization methods, perturbed physics and forcing, but they had different realizations. We built multi-model ensemble mean responses on forcing to overcome uncertainties. Before assessing D&A analysis, we analysed the relationship between indices and ENSO events. Moreover, we compared CMIP6 ensemble members under ALL, GHG, ANT and NAT forcings with observations using the Taylor diagram method. Finally, we made spatial and temporal comparisons between observed and model simulation trends over 1950–2018.

Our findings are consistent with those for the global and regional scales. The observed indices trends were consistent with our previous analysis (Randriamarolaza et al., 2021). However, this article was completed with a brief assessment of ENSO's influence on indices by using wavelet coherence method. As underlined by Dong et al. (2018) for Asia, warm event changes were also more pronounced after the 1980s. On the other hand, the influence of external forcing was detectable in observations for intensity and frequency indices in temperature extremes over 1950–2018 in Madagascar. Mostly, observed changes of intensity and frequency indices were attributed to GHG and ANT forcings. These results were mostly consistent with Global and Europe results over 1961–2010 and Asia results over 1958–2012 found by Christidis and Stott (2016) and Dong et al. (2018), respectively. However, the influence of GHG forcing on TNn and TXn were not detected in Europe. The influence of ALL forcing on TNx, TXx, TNn and TXn were not credible in Asia for lower and higher latitudes, respectively. Moreover, regional average index trend behaviours were comparable to Globally and European average index trends in Christidis and Stott (2016). For percentile-based indices, Morak et al. (2013) found similar warming trends by telling that TX10P, TX90P, TN10P and TN90P decreased and increased over 1951–2013, respectively. These observed changes were influenced by external forcing at 5% level. Noticed that Morak et al. (2013) and Christidis and Stott (2016) did not adopt a multi-model approach but they employed indices directly with optimal fingerprinting method. Nevertheless, Min et al. (2013) and Kim et al. (2016) employed a multi-model approach, but they transformed variables to probability-based index before applying standard optimal fingerprinting methods. They found that observed changes of TXn, TXx, TNn and TXx were influenced by external forcing. Then Kim et al. (2016) observed that CMIP5 models agreed better with observed changes in TNx and TXx than the previous study with CMIP3. We also found similar agreement between CMIP6 models and observed changes, especially for frequency indices in Madagascar.

We recognize, as a setback of this article, that we did not evaluate model performance at regional levels. Moreover, individual model numbers might be insufficient. However, we selected ensemble members with similar initialization methods, perturbed physics and forcing. Besides, index regional time series of OBS, ALL, GHG, ANT and NAT forcings were compared to capture their evolution (see Figures 6 and 7). But we might add the validation of models against observation as adopted by Otto et al. (2013) to improve our results. Therefore, this research might be improved by tackling these gaps issues and implementing standard optimal fingerprinting methods with a

probability-based index or extreme value theory. We might also extend the study with other indices (e.g., indices related to precipitation). However, it was important to think about how to apply these findings on real time to assess actual risks by connecting them to sector impacts such as agriculture, health and so on.

AUTHOR CONTRIBUTIONS

Luc Yannick Andréas RANDRIAMAROLAZA: Conceptualization; data curation; formal analysis; investigation; methodology; software; validation; visualization; writing – original draft; writing – review and editing. **Enric Aguilar:** Conceptualization; formal analysis; funding acquisition; methodology; project administration; supervision; validation; writing – review and editing. **Oleg Skrynyk:** Conceptualization; formal analysis; methodology; validation; writing – review and editing.

ACKNOWLEDGEMENTS

This study was not completed without the climate data from Directorate General of Meteorology of Madagascar and the financial support from the INDECIS project. It is a part of ERA4CS, an ERA-NET initiated by JPI Climate, and funded by FORMAS (SE), DLR (DE), BMWFW (AT), IFD (DK), MINECO (ES), ANR (FR) with co-funding by the European Union (Grant 690462). The authors thank all those who helped to improve this study, particularly Xuebin Zhang and the anonymous reviewers for their in-depth reading of the manuscript and their valuable comments and suggestions.

ORCID

Luc Yannick Andréas Randriamarolaza https://orcid.org/0000-0002-2939-2250
Enric Aguilar https://orcid.org/0000-0002-8384-377X
Oleg Skrynyk https://orcid.org/0000-0001-8827-0280

REFERENCES

Allen, M.R. & Stott, P.A. (2003) Estimating signal amplitudes in optimal fingerprinting, Part I: theory. *Climate Dynamics*, 21, 477–491. Available from: https://doi.org/10.1007/s00382-003-0313-9

Allen, M.R. & Tett, S.F.B. (1999) Checking for model consistency in optimal fingerprinting. *Climate Dynamics*, 15, 419–434. Available from: https://doi.org/10.1007/s003820050291

Barry, A.A., Caesar, J., Klein, T.A.M.G., Aguilar, E., McSweeney, C., Cyrille, A.M. et al. (2018) West Africa climate extremes and climate change indices. *International Journal of Climatology*, 38, e921–e938. Available from: https://doi.org/10.1002/joc.5420

Bindoff, N.L., Stott, P.A., Achuta Rao, K.M., Allen, M.R., Gillett, N., Gutzler, D. et al. (2013) Detection and attribution of climate change: from global to regional. In: Stocker, T.F., Qin, D., Plattner, G.K., Tignor, M., Allen, S.K., Boschung, J. et al. (Eds.) *Climate Change 2013: The Physical Science Basis. Contribution of Working Group I to the Fifth Assessment Report of the Intergovernmental Panel on Climate Change*. Cambridge, UK; New York, NY: *Cambridge University Press*. Available from: https://doi.org/10.1017/CBO9781107415324.022

Bronaugh, D. & Werner, A. (2019) Package 'zyp'. https://CRAN.R-project.org/package=zyp

Christidis, N. & Stott, P.A. (2016) Attribution analyses of temperature extremes using a set of 16 indices. *Weather and Climate Extremes*, 14, 24–35. Available from: https://doi.org/10.1016/j.wace.2016.10.003

Coumou, D. & Rahmstorf, S. (2012) A decade of weather extremes. *Nature Climate Change*, 2, 491–496. Available from: https://doi.org/10.1038/nclimate1452

Curry, J.A. & Webster, P.J. (2011) Climate science and the uncertainty monster. *Bulletin of the American Meteorological Society*, 92, 1667–1682. Available from: https://doi.org/10.1175/2011BAMS3139.1

Dileepkumar, R., AchutaRao, K. & Arulalan, T. (2018) Human influence on sub-regional surface air temperature change over India. *Scientific Reports*, 8, 8967. Available from: https://doi.org/10.1038/s41598-018-27185-8

Dima, M., Lohmann, G. & Dima, I. (2005) Solar-induced and internal climate variability at decadal time scales. *International Journal of Climatology*, 25(6), 713–733. Available from: https://doi.org/10.1002/joc.1156

Domínguez-Castro, F., Reig, F., Vicente-Serrano, S.M., Aguilar, E., Peña-Angulo, D., Noguera, I. et al. (2020) A multidecadal assessment of climate indices over Europe. *Scientific Data*, 7, 125. Available from: https://doi.org/10.1038/s41597-020-0464-0

Dong, S., Sun, Y., Aguilar, E., Zhang, X., Peterson, T.C., Song, L. et al. (2018) Observed changes in temperature extremes over Asia and their attribution. *Climate Dynamics*, 51, 339–353. Available from: https://doi.org/10.1007/s00382-017-3927-z

Eyring, V., Bony, S., Meehl, G.A., Senior, C.A., Stevens, B., Stouffer, R.J. et al. (2016) Overview of the Coupled Model Intercomparison Project Phase 6 (CMIP6) experimental design and organization. *Geoscientific Model Development*, 9, 1937–1958. Available from: https://doi.org/10.5194/gmd-9-1937-2016

Gillett, N.P., Shiogama, H., Funke, B., Hegerl, G., Knutti, R., Matthes, K. et al. (2016) The Detection and Attribution Model Intercomparison Project (DAMIP v1.0) contribution to CMIP6. *Geoscientific Model Development*, 9, 3685–3697. Available from: https://doi.org/10.5194/gmd-9-3685-2016

Grinsted, A., Moore, J.C. & Jevrejeva, S. (2004) Application of the cross wavelet transform and wavelet coherence to geophysical time series. *Nonlinear Processes in Geophysics*, 11, 561–566. Available from: https://doi.org/10.5194/npg-11-561-2004

Hannart, A., Ribes, A. & Naveau, P. (2014) Optimal fingerprinting under multiple sources of uncertainty. *Geophysical Research Letters*, 41, 1261–1268. Available from: https://doi.org/10.1002/2013GL058653

Hegerl, G. & Zwiers, F. (2011) Use of models in detection and attribution of climate change. *WIREs Climate Change*, 2, 570–591. Available from: https://doi.org/10.1002/wcc.121

Huang, B., Thorne, P.W., Banzon, V.F., Boyer, T., Chepurin, G., Lawrimore, J.H. et al. (2017) Extended Reconstructed Sea Surface Temperature, Version 5 (ERSSTv5): upgrades, validations,

and intercomparisons. *Journal of Climate*, 30, 8179–8205. Available from: https://doi.org/10.1175/JCLI-D-16-0836.1

Jevrejeva, S., Moore, J.C. & Grinsted, A. (2003) Influence of the Arctic Oscillation and El Niño-Southern Oscillation (ENSO) on ice conditions in the Baltic Sea: the wavelet approach. *Journal of Geophysical Research: Atmospheres*, 108(21), 1–11. Available from: https://doi.org/10.1029/2003jd003417

Kim, Y.H., Min, S.K., Zhang, X., Zwiers, F., Alexander, L.V., Donat, M.G. et al. (2016) Attribution of extreme temperature changes during 1951–2010. *Climate Dynamics*, 46, 1769–1782. Available from: https://doi.org/10.1007/s00382-015-2674-2

Liang, L., Li, L., Liu, C. & Cuo, L. (2013) Climate change in the Tibetan Plateau Three Rivers Source Region: 1960–2009. *International Journal of Climatology*, 33, 2900–2916. Available from: https://doi.org/10.1002/joc.3642

Lilly, J.M. (2017) Element analysis: a wavelet-based method for analysing time-localized events in noisy time series. *Proceedings of the Royal Society A: Mathematical, Physical and Engineering Sciences*, 473, 20160776. Available from: https://doi.org/10.1098/rspa.2016.0776

Lo, Y., Charlton-Perez, A., Lott, F. & Highwood, E. (2016) Detecting sulphate aerosol geoengineering with different methods. *Scientific Reports*, 6, 39169. Available from: https://doi.org/10.1038/srep39169

Lu, C., Sun, Y. & Zhang, X. (2018) Multimodel detection and attribution of changes in warm and cold spell durations. *Environmental Research Letters*, 13(7), 074013. Available from: https://doi.org/10.1088/1748-9326/aacb3e

Meinshausen, M., Vogel, E., Nauels, A., Lorbacher, K., Meinshausen, N., Etheridge, D.M. et al. (2017) Historical greenhouse gas concentrations for climate modelling (CMIP6). *Geoscientific Model Development*, 10(5), 2057–2116. Available from: https://doi.org/10.5194/gmd-10-2057-2017

Min, S.K., Zhang, X., Zwiers, F., Shiogama, H., Tung, Y.S. & Wehner, M. (2013) Multimodel detection and attribution of extreme temperature changes. *Journal of Climate*, 26, 7430–7451. Available from: https://doi.org/10.1175/jcli-d-12-00551.1

Morak, S., Hegerl, G.C. & Christidis, N. (2013) Detectable changes in the frequency of temperature extremes. *Journal of Climate*, 26, 1561–1574. Available from: https://doi.org/10.1175/JCLI-D-11-00678.1

Morak, S., Hegerl, G.C. & Kenyon, J. (2011) Detectable regional changes in the number of warm nights. *Geophysical Research Letters*, 38, L17703. Available from: https://doi.org/10.1029/2011GL048531

O'Neill, B.C., Tebaldi, C., van Vuuren, D.P., Eyring, V., Friedlingstein, P., Hurtt, G. et al. (2016) The Scenario Model Intercomparison Project (ScenarioMIP) for CMIP6. *Geoscientific Model Development*, 9, 3461–3482. Available from: https://doi.org/10.5194/gmd-9-3461-2016

Otto, F.E.L., Boyd, E., Jones, R.G., Cornforth, R.J., James, R., Parker, H.R. et al. (2015) Attribution of extreme weather events in Africa: a preliminary exploration of the science and policy implications. *Climatic Change*, 132, 531–543. Available from: https://doi.org/10.1007/s10584-015-1432-0

Otto, F.E.L., Harrington, L., Schmitt, K., Philip, S., Kew, S., van Oldenborgh, G.J. et al. (2020) Challenges to understanding extreme weather changes in lower income countries. *Bulletin of the American Meteorological Society*, 101, E1851–E1860. Available from: https://doi.org/10.1175/BAMS-D-19-0317.1

Otto, F.E.L., Jones, R.G., Halladay, K. & Allen, M.R. (2013) Attribution of changes in precipitation patterns in African Rainforests. *Philosophical Transactions of the Royal Society B: Biological Sciences*, 368, 20120299. Available from: https://doi.org/10.1098/rstb.2012.0299

Peterson, T.C., Hoerling, M.P., Stott, P.A. & Herring, S.C. (2013) Explaining extreme events of 2012 from a climate perspective. *Bulletin of the American Meteorological Society*, 94, S1–S74. Available from: https://doi.org/10.1175/BAMS-D-13-00085.1

Peterson, T.C., Stott, P.A. & Herring, S.C. (2012) Explaining extreme events of 2011 from a climate perspective. *Bulletin of the American Meteorological Society*, 93, 1041–1067. Available from: https://doi.org/10.1175/BAMS-D-12-00021.1

Randriamarolaza, L.Y.A., Aguilar, E., Skrynyk, O., Vicente-Serrano, S.M. & Domínguez-Castro, F. (2021) Indices for daily temperature and precipitation in Madagascar, based on quality-controlled and homogenized data, 1950–2018. *International Journal of Climatology.*, 42, 265–288. Available from: https://doi.org/10.1002/joc.7243

Ribes, A., Planton, S. & Terray, L. (2013) Application of regularised optimal fingerprinting to attribution. Part I: method, properties and idealised analysis. *Climate Dynamics*, 41, 2817–2836. Available from: https://doi.org/10.1007/s00382-013-1735-7

Ruwangika, A.M., Perera, A. & Rathnayake, U. (2020) Comparison of statistical, graphical, and wavelet transform analyses for rainfall trends and patterns in Badulu Oya Catchment, Sri Lanka. *Complexity*, 2020, 7146593. Available from: https://doi.org/10.1155/2020/7146593

Santer, B.D., Wigley, T.M.L., Barnett, T.P. & Anyamba, E. (1996) Detection of climate change and attribution of causes. In: *Climate Change 1995: The Science of Climate Change. Contribution of Working Group I to the Second Assessment Report of the Intergovernmental Panel on Climate Change*, Vol. 30. Cambridge, UK: Cambridge Unversity Press, pp. 91–109. Available from: https://doi.org/10.4324/9780203876213.ch1

Santoso, A., Mcphaden, M.J. & Cai, W. (2017) The defining characteristics of ENSO extremes and the strong 2015/2016 El Niño. *Reviews of Geophysics*, 55, 1079–1129. Available from: https://doi.org/10.1002/2017RG000560

Sen, P.K. (1968) Estimates of the regression coefficient based on Kendall's tau. *Journal of the American Statistical Association*, 63, 1379–1389. Available from: https://doi.org/10.1080/01621459.1968.10480934

Skrynyk, O., Aguilar, E., Guijarro, J., Randriamarolaza, L.Y.A. & Bubin, S. (2021) Uncertainty evaluation of Climatol's adjustment algorithm applied to daily air temperature time series. *International Journal of Climatology*, 41, E2395–E2419. Available from: https://doi.org/10.1002/joc.6854

Sonali, P. & Kumar, D.N. (2020) Review of recent advances in climate change detection and attribution studies: a large-scale hydroclimatological perspective. *Journal of Water and Climate Change*, 11, 1–29. Available from: https://doi.org/10.2166/wcc.2020.091

Stott, P.A., Jones, G.S., Christidis, N., Zwiers, F.W., Hegerl, G. & Shiogama, H. (2011) Single-step attribution of increasing frequencies of very warm regional temperatures to human influence. *Atmospheric Science Letters*, 12, 220–227. Available from: https://doi.org/10.1002/asl.315

Swart, N.C., Cole, J.N.S., Kharin, V.V., Lazare, M., Scinocca, J.F., Gillett, N.P. et al. (2019) The Canadian Earth System Model

version 5 (CanESM5.0.3). *Geoscientific Model Development*, 12, 4823–4873. Available from: https://doi.org/10.5194/gmd-12-4823-2019

Tarik, C.G., Grinsted, A. & Simko, V. (2018) *R package biwavelet: Conduct Univariate and Bivariate Wavelet Analyses (Version 0.20.17)*. Available at: https://github.com/tgouhier/biwavelet

Taylor, K.E. (2001) Summarizing multiple aspects of model performance in a single diagram. *Journal of Geophysical Research Atmospheres*, 106(D7), 7183–7192. Available from: https://doi.org/10.1029/2000JD900719

Torrence, C. & Compo, G. (1998) A practical guide to wavelet analysis. *Bulletin of the American Meteorological Society*, 79, 61–78. Available from: https://doi.org/10.1175/1520-0477(1998)079<0061:APGTWA>2.0.CO;2

Vincent, L.A., Aguilar, E., Saindou, M., Hassane, A.F., Jumaux, G., Roy, D. et al. (2011) Observed trends in indices of daily and extreme temperature and precipitation for the countries of the western Indian Ocean, 1961–2008. *Journal of Geophysical Research-Atmospheres*, 116(10), 1–12. Available from: https://doi.org/10.1029/2010JD015303

Wan, H., Zhang, X., Zwiers, F. & Min, S.K. (2014) Attributing northern high-latitude precipitation change over the period 1966–2005 to human influence. *Climate Dynamics*, 45, 1713–1726. Available from: https://doi.org/10.1007/s00382-014-2423-y

Wang, Z., Jiang, Y., Wan, H., Yan, J. & Zhang, X. (2020) Toward optimal fingerprinting in detection and attribution of changes in climate extremes. *Journal of the American Statistical Association*, 116, 1–13. Available from: https://doi.org/10.1080/01621459.2020.1730852

Yi, H. & Shu, H. (2012) The improvement of the Morlet wavelet for multi-period analysis of climate data. *Comptes Rendus Geoscience*, 344, 483–497. Available from: https://doi.org/10.1016/j.crte.2012.09.007

Yosef, Y., Aguilar, E. & Alpert, P. (2019) Changes in extreme temperature and precipitation indices: using an innovative daily homogenized database in Israel. *International Journal of Climatology*, 39, 5022–5045. Available from: https://doi.org/10.1002/joc.6125

Yosef, Y., Aguilar, E. & Alpert, P. (2020) Is it possible to fit extreme climate change indices together seamlessly in the era of accelerated warming? *International Journal of Climatology*, 41, E952–E963. Available from: https://doi.org/10.1002/joc.6740

Zhai, P., Zhou, B. & Chen, Y. (2018) A review of climate change attribution studies. *Journal of Meteorological Research*, 32, 671–692. Available from: https://doi.org/10.1007/s13351-018-8041-6

Zhang, X., Vincent, L.A., Hogg, W.D. & Niitsoo, A. (2000) Temperature and precipitation trends in Canada during the 20th century. *Atmosphere-Ocean*, 38, 395–429. Available from: https://doi.org/10.1080/07055900.2000.9649654

Zhang, X., Wan, H., Zwiers, F.W., Hegerl, G.C. & Min, S.K. (2013) Attributing intensification of precipitation extremes to human influence. *Geophysical Research Letters*, 40, 5252–5257. Available from: https://doi.org/10.1002/grl.51010

How to cite this article: Randriamarolaza, L. Y. A., Aguilar, E., & Skrynyk, O. (2023). Extreme temperatures detection and attribution related to external forcing in Madagascar. *International Journal of Climatology*, *43*(8), 3907–3924. https://doi.org/10.1002/joc.8065